Sustainable Energy & Fuels

ROYAL SOCIETY OF CHEMISTRY

PAPER

View Article Online
View Journal | View Issue

Cite this: *Sustainable Energy Fuels*, 2026, **10**, 1093

Synergistic plasmonic–semiconductor heterointerfaces enabling efficient CO_2 hydrogenation to methanol under visible-light irradiation

Abdul Malek,[ac] Anh-Tuan Hoang,[d] Md. Tarekul Islam,[e] Mohammad A. Hasnat,[f] Tarikul Islam *[g] and Aminul Islam *[abc]

The photocatalytic conversion of carbon-dioxide (CO_2) to methanol (CH_3OH) under mild conditions has been regarded as a promising, cost-effective, and environmentally sustainable approach for carbon utilization and renewable fuel generation. However, the process has been hindered by limited charge separation efficiency and insufficient CO_2 activation. In this study, a heterostructured Ag–Si/MgO/ZnO photocatalyst was rationally designed and synthesized *via* a solid-phase reaction method. A CH_3OH production rate of 357.53 μmol g_{cat}^{-1} h^{-1} was achieved over the optimized 10% Ag–Si/MgO/ZnO composite catalyst at 250 °C, representing a substantial enhancement compared to the Si/ZnO and Si/MgO/ZnO photocatalysts. The CH_3OH production performance was found to be higher in the photocatalyst/gas-phase system than that reported in comparable studies. The theoretical activation energy for Ag–Si/MgO/ZnO was found to be 158.14 kJ mol^{-1}, which is lower than that of Si/MgO/ZnO (167.79 kJ mol^{-1}) and Si/ZnO (177.97 kJ mol^{-1}), indicating enhanced CO_2 activation and higher CO_2 conversion. More importantly, after more than 72 h of irradiation, the system still exhibited a high CH_3OH production rate, demonstrating its potential for practical application.

Received 17th November 2025
Accepted 7th January 2026

DOI: 10.1039/d5se01485a

rsc.li/sustainable-energy

1. Introduction

The average concentration of CO_2 has jumped to 427.48 ppm in the atmosphere currently,[1] although the concentration level of CO_2 in the atmosphere shouldn't be higher than 350 ppm. The sharp increase in concentration of CO_2 in the atmosphere is the main driver of the greenhouse effect which causes global warming and climate change, gravely affecting the ability of human beings to live normally. Therefore, limiting the release of CO_2 is a significant task for humankind in an attempt to mitigate global warming. The production of liquid fuels and value-added chemicals *via* CO_2 hydrogenation has recently gained significant attention due to its promising economic potential and environmental advantages.[2–4] Various value-added chemicals including CH_3OH, CH_4, CH_3CH_2OH, olefins, DME *etc.* are obtained from hydrogenation of CO_2.[5,6] Among different products, CH_3OH has extensive applications as a vital organic solvent. It is an essential organic feedstock for organic synthesis, including the production of HCHO, $C_3H_6O_3$, C_2H_4, CH_3COOH, and other substances. It is also used as a hydrogen carrier, an energy source for fuel cells, and a feedstock for gasoline production.[7,8] Consequently, the process of hydrogenation of CO_2 into CH_3OH utilizing green H_2 has garnered a lot of interest recently.[9,10]

CO_2 hydrogenation to CH_3OH had been extensively studied. For instance, new active sites were introduced through nitrogen doping by Yang *et al.*,[11] which resulted in significant enhancement of reaction activity and catalytic stability of In_2O_3. Using an In_2O_3 nano-catalyst, a CH_3OH selectivity of 62.3% was achieved at 300 °C and 5 MPa. The ZrO_2/Cu photocatalyst was reported to have exhibited strong activity for CH_3OH formation. The hydrogenation of surface oxygenate intermediates and the activation of CO_2 were found to have been significantly enhanced over these configurations. In Cu-based catalysts, the promotion of CH_3OH synthesis was observed when Zn species were incorporated. The presence of Zn species was found to have increased the dispersion of Cu particles and prevented

[a]*Department of Petroleum and Mining Engineering, Jashore University of Science and Technology, Jashore 7408, Bangladesh. E-mail: aminul_pme@just.edu.bd*

[b]*College of Engineering, Korea University, 145 Anam-ro, Seongbuk-gu, Seoul 02841, Republic of Korea*

[c]*Hydrogen Energy and CO_2 Conversion Lab, Department of Petroleum and Mining Engineering, Jashore University of Science and Technology, Jashore 7408, Bangladesh*

[d]*Energy-Fuel Technology and Applied Material Research Group, Dong Nai Technology University, Dong Nai, Vietnam*

[e]*Department of Leather Engineering, Faculty of Mechanical Engineering, Khulna University of Engineering and Technology, Khulna 9203, Bangladesh*

[f]*Department of Chemistry, School of Physical Sciences, Shahjalal University of Science and Technology, Sylhet 3114, Bangladesh*

[g]*Department of Textiles, Merchandising, and Interiors, University of Georgia, Athens, Georgia 30602, USA. E-mail: tarikul@uga.edu*

their agglomeration. As a result, a high copper surface area was maintained on the catalyst, which was considered to have improved its performance in CH_3OH synthesis. Moreover, the incorporation of ZnO was observed to have strengthened the resistance of Cu particles to poisoning, improved CO_2 adsorption on the catalyst surface, and provided a higher density of catalytically active sites for the reactants.

Single-component photocatalysts had typically been limited by poor visible-light utilization, fast electron–hole recombination, and unfavorable adsorption energetics for key CO_2-reduction intermediates, whereas complementary metals had been shown to adjust charge-transfer pathways and intermediate binding in a controllable manner.[12] In bimetallic systems, plasmonic nanoparticles had been expected to generate localized surface plasmon resonance under visible light. As a result, hot-carrier generation and near-field enhancement had been exploited to strengthen light excitation and accelerate electron injection into nearby semiconductor or oxide domains, as widely reported for plasmon-assisted CO_2 photoreduction.[13] Meanwhile, semiconductor domains had been introduced to tune the interfacial electronic structure and adsorption behavior. This approach had allowed early oxygenated intermediates to be stabilized on oxide sites, while hydrogenation-favored steps had been promoted on plasmonic metal sites, in agreement with the principle that bimetallic interfaces enabled spatial separation of adsorption/activation and hydrogenation functions.[14] This mechanism had been expected to enhance both activity and selectivity by increasing the supply of reactive electrons from plasmonic components and by optimizing intermediate binding while suppressing unproductive pathways through interfacial site differentiation.[15]

Elemental Si, a visible-light-responsive semiconductor with a narrow indirect bandgap of ~1.1 eV, enables broad solar absorption and efficient generation of charge carriers under light irradiation, making it highly suitable for solar-driven catalytic applications.[16] When coupled with plasmonic components, Si primarily functions as an electron reservoir and transport medium, facilitating the directional migration of photogenerated or plasmon-induced hot electrons toward catalytically active surface sites. This process promotes interfacial charge separation and effectively suppresses electron–hole recombination through plasmonic–semiconductor coupling and Schottky junction formation.[17] Similar Si-based photocatalytic architectures have been reported to enhance visible-light utilization, charge separation efficiency, and CO_2 reduction performance through plasmonic–semiconductor coupling effects.[18,19] Plasmonic–semiconductor photocatalysts can utilize up to ~45% of the solar spectrum, significantly improving photon-to-chemical conversion efficiency and reducing external heating energy input.[20] By coupling localized surface plasmon resonance (LSPR)–induced hot-electron generation with semiconductor charge transport, the system drives CO_2 reduction under mild conditions, thus lowering operational energy requirements per unit methanol produced. From a techno-economic perspective, visible-light-assisted pathways may become cost-competitive as renewable H_2 prices continue to decline and scalable synthesis routes for plasmonic materials (*e.g.*, Ag and Cu) are further optimized.[21] Recent analyses suggest that photocatalytic methanol production can be economically favorable when solar-to-fuel efficiencies exceed 5–8% and catalyst stability surpasses several thousand hours.[22] Although further development is needed, the combination of low-temperature operation and reduced energy intensity, and the prospect of using abundant, sunlight-driven excitation underscore the long-term economic viability of plasmonic–semiconductor photocatalysts for sustainable CO_2 valorization.

Visible-light-driven CH_3OH synthesis over plasmonic Cu/ZnO catalysts, achieving a CH_3OH production rate of 127.8 $\mu mol\ g^{-1}\ h^{-1}$, was reported by Wang and co-workers.[23] It was found that, despite these advancements, copper-based catalysts were still prone to favor the reverse water–gas shift (RWGS) reaction. This undesired pathway was identified as a major limitation to the selective hydrogenation of CO_2 into CH_3OH and other value-added products when thermal heterogeneous catalysts were employed. To mitigate sintering and enhance catalyst stability, various promoters such as Al_2O_3, MgO, SiO_2, CeO_2, and ZrO_2 were commonly incorporated.[24] Among these, MgO was recognized as a promising promoter owing to its unique physicochemical properties. MgO was reported to inhibit the RWGS reaction and function as an adsorbent carrier with desirable features such as large surface area, high density of adsorption sites, tunable surface properties, and high chemical reactivity. Mg-based catalysts were reported to exhibit excellent performance for CO_2 hydrogenation to hydrocarbons. The incorporation of MgO as a catalyst component led to enhanced CO_2 adsorption due to its basic nature and improved metal dispersion by increasing surface area as a result of its low density. Few studies had been conducted on MgO-based catalysts for CO_2 hydrogenation to CH_3OH, and MgO was generally combined with other catalytic components to improve overall performance. For example, the influence of $Cu/MgO/Al_2O_3$ catalysts was investigated by Dasireddy *et al.*,[25] and the $Cu/MgO/Al_2O_3$ sample was reported to display the highest activity, which was attributed to the increased number of active sites for CO_2 and H_2 adsorption provided by MgO. Using a Cu–ZnO/MgO catalyst, Guo *et al.* achieved a CO_2 conversion of 7.6% and a CH_3OH selectivity of 91% at 200 °C and 5 MPa.[26] These findings demonstrated that high CH_3OH selectivity could be achieved through conventional heterogeneous catalysis. Nevertheless, because of the inherent thermodynamic stability of CO_2, its hydrogenation to CH_3OH was typically carried out under relatively harsh conditions, requiring elevated temperatures (>200 °C) and high pressures (>4 MPa).

Doping was adopted as a standard modification strategy and was increasingly focused upon by researchers. Among the various modification approaches applied to ZnO or MgO carriers, the incorporation of metals was predominantly employed. Noble metals were considered effective cocatalysts for charge carrier separation, as they were believed to act as electron sinks and solid-state mediators. Catalysts based on noble metals such as Pd, Pt, and Au were reported to exhibit excellent hydrogen spillover capacity, high stability, and strong anti-sintering ability in the CO_2-to-CH_3OH reaction.[27] For

instance, oxygen vacancies were introduced on the surface of Pd/In_2O_3 catalysts by Men *et al.*,[28] resulting in a CH_3OH yield of 8.9% with a CO_2 conversion of 24.5%. Similarly, a 2 wt% Pd/CeO_2 catalyst was reported by Pothu *et al.* to have achieved a CO_2 conversion of 49.6% and a CH_3OH selectivity of 69.5%.[29] In another study, CO_2 hydrogenation with H_2 over a Pt/film/In_2O_3 catalyst was reported by Men and co-workers,[28] achieving a CO_2 conversion of 37.0% and a CH_3OH selectivity of 62.6%. Sun *et al.* confirmed,[30] both theoretically and experimentally, the feasibility of selective CO_2 hydrogenation to CH_3OH over Ag/In_2O_3. Under reaction conditions of 300 °C and 5 MPa, a CH_3OH selectivity of 58.2% was maintained with a CO_2 conversion of 13.6% and a space–time yield (STY) of 0.453 $g_{methanol}\ g^{-1}\ h^{-1}$. The appropriate selection of a metal for doping into the metal oxide catalyst was reported to enhance interfacial charge transfer, thereby significantly improving CO_2 adsorption. Although plasmonic–semiconductor hybrid systems have been investigated under photothermal conditions, where thermal effects predominantly govern the catalytic activity,[31–34] studies focusing on photocatalytic CO_2 conversion driven by plasmon-induced charge separation particularly in silicon-based, cost-effective semiconductor platforms remain limited.

In this study, a plasmonic Ag–Si/MgO/ZnO composite photocatalyst was synthesized *via* a solid-phase reaction method, and its photocatalytic performance was evaluated for CO_2 conversion under visible-light irradiation. Bimetallic Ag and Si species were introduced as cocatalysts supported on an MgO promoter to enhance charge separation efficiency and overall catalytic activity of the Ag–Si/MgO/ZnO system. The photocatalytic performance was systematically investigated in terms of product yield and apparent quantum yield (AQY). Furthermore, surface activation, structural evolution, and catalyst stability under extended illumination were analyzed using a suite of advanced characterization techniques. The findings reveal that the engineered heterostructure exhibits excellent stability, high photocatalytic efficiency, and strong scalability potential, offering valuable insights into the rational design of next-generation plasmonic–semiconductor systems for solar-driven CO_2 reduction.

2. Materials and methods

2.1 Materials

Mg powder (99%), Zn powder (99%), silver nitrate ($AgNO_3$), tri-sodium citrate dehydrate ($C_6H_5Na_3O_7 \cdot 2H_2O$), and sodium borohydride ($NaBH_4$) were purchased from Sigma-Aldrich (USA). Ultra-pure water was supplied through distillation of water. CO_2 (99.99%) and N_2 (99.99%) were collected from Spectra International Limited, Bangladesh. Water is electrolyzed to deliver renewable H_2 (99.99%). The electrolyte, Na_2SO_4 (99.99%) utilized to electrolyze water, was purchased from Sigma-Aldrich (USA). All chemicals used in this work were employed without any additional treatment.

2.2 Synthesis of SiO_2

Through the calcination procedure, waste rice husk was converted into a precursor silica (SiO_2) nanopowder. The wasted rice husk was first acid purified by immersing it in a 1000 mL aqueous solution of 20% HCl in a beaker and heating it to 100 °C for six hours. After being cleaned three times with pure water, the deep yellow rice husk was taken out from the beaker. The cleaned rice husk was then dried in an oven for 12 hours at 90 °C. To calcine the sample, the dried rice husk was placed in a tube furnace with the aid of a ceramic crucible and heated to 800 °C for two hours at a ramping rate of 10 °C min^{-1}. The bright white SiO_2 powder was collected when it had reached room temperature.

2.3 Synthesis of Si/MgO/ZnO

To develop a semiconductor-based photocatalyst, the solid combustion approach was utilized in a specifically developed sealed stainless steel reactor. Employing a single-step magneto-thermic reduction technique, a Si/MgO/ZnO composite was developed in an enclosed reactor. Initially, 1 g of the obtained SiO_2 nanopowder was finely ground with 0.65 g of Zn powder and 0.65 g of Mg powder by with the proportions of SiO_2, Zn, and Mg being 1 : 0.65 : 0.65. Then, the sealed stainless steel reactor was filled with the ground mixture of SiO_2, Zn, and Mg powders. To execute the magneto-thermic conversion, the enclosed stainless steel reactor was placed within a muffle furnace and heated to 800 °C for 6 h, increasing the temperature by 5 °C per minute. The reactor was removed from the furnace once it reached room temperature. The built Si/MgO/ZnO material was removed from the reactor and finely powdered.

2.4 Synthesis of Ag nanoparticles (NPs)

Ag nanoparticles (Ag NPs) were synthesized *via* a chemical reduction method employing tri-sodium citrate ($C_6H_5Na_3O_7 \cdot 2H_2O$) and sodium borohydride ($NaBH_4$) as reducing agents. Silver nitrate ($AgNO_3$) and $Na_3C_6H_5O_7$ were used as precursors, and all solutions were freshly prepared using distilled water. In a typical procedure, 100 mL of 1 M $Na_3C_6H_5O_7$ solution was magnetically stirred, after which 100 mL of 0.25 mM $AgNO_3$ solution was added dropwise under continuous stirring until a clear and homogeneous solution was obtained. Subsequently, 250 mL of 148 mM $NaBH_4$ solution was introduced dropwise at a controlled rate of approximately one drop per second. The reaction mixture was stirred vigorously for 6 h, during which a gradual color transition from light yellow to dark yellow and finally to gray was observed, indicating nanoparticle formation and subsequent colloid destabilization. After completion of the reaction, stirring was stopped, and the solution was left undisturbed overnight to allow complete precipitation of the nanoparticles. The resulting Ag nanoparticles had been collected as a solid residue, repeatedly washed with distilled water to remove impurities, and subsequently subjected to high-temperature treatment (850 °C for 6 h) during photocatalyst preparation. Therefore, any residual species would have been expected to be removed through the post calcination process.

2.5 Synthesis of Ag–Si/MgO/ZnO

With the aid of a hydraulic pressure machine, the fine Ag–Si/MgO/ZnO mixture powder was further sealed in a cylindrical

stainless steel reactor under elevated pressures. Attempting to build a solid Ag–Si/MgO/ZnO structure, the reactor was then placed inside a muffle furnace and heated to 850 °C for 6 h, increasing the temperature by 5 °C per minute. When the reactor reached room temperature, it was removed from the furnace. Employing a hydraulic pressure machine, the Ag–Si/MgO/ZnO specimen with a solid structure was removed from the reactor. After the surface of the formed solid Ag–Si/MgO/ZnO specimen was cleaned with emery paper, it was heated in a muffle furnace for two hours at a temperature of 5 °C per minute. The solid-structured Ag–Si/MgO/ZnO composite was subsequently removed from the furnace and split it into several pieces to be used as a photocatalyst in a continuous flow reactor once it had reached room temperature. To assess the photocatalytic efficiency, additional Si/MgO/ZnO and Si/ZnO catalysts were developed without Ag or Ag/MgO, respectively. The overall synthesis process of the Ag–Si/MgO/ZnO photocatalyst is presented in Fig. S1.

2.6 Characterization

The microstructure and morphology of the prepared materials were characterized by scanning electron microscopy (SEM, Sigma-300, Germany), while elemental composition and mapping were determined by energy-dispersive spectroscopy (EDS). Transmission electron microscopy (TEM) and high-resolution TEM (HRTEM) images with elemental mapping were obtained using FEI Talos F200X and Tecnai F20 instruments. The crystalline phases were analyzed by X-ray diffraction (XRD, Bruker AXS, Germany) using Cu Kα radiation ($\lambda = 1.5418$ Å). Optical absorbance and diffuse reflectance spectra were recorded using a Cary 5000 UV-vis spectrophotometer (Varian, USA) and a Thermo Scientific Evolution 220 UV-vis DRS instrument, respectively. Surface composition and chemical states were examined by X-ray photoelectron spectroscopy (XPS, ESCALAB 250Xi, Thermo Fisher, UK), and photoluminescence (PL) spectra of the solid powders were measured with a Hitachi F-7000 fluorescence spectrophotometer (Japan).

2.7 Photo-electrochemical tests

A CorrTest electrochemical workstation (Wuhan Corrtest Instruments Comp. Ltd, China) was utilized to measure the transient photocurrent response of all samples. The electrochemical impedance spectroscopy and Mott–Schottky plots of catalyst specimens were performed on an Autolab workstation (Netherlands). A platinum wire served as the counter electrode. An Ag/AgCl electrode was used as the reference electrode. A conventional quartz cell with three electrodes was employed in both the electrochemical systems. A solution of 0.5 M Na_2SO_4 was used as the electrolyte. The series of photocatalyst films were coated on fluorine-tin-oxide (FTO) glasses of 1 cm^2 area and used as a working electrode. The working electrodes were prepared using the doctor blade method. In short, before preparing the solution, the polyvinylidene difluoride (PVDF) binder was dried over an entire night. *N*-Methyl-2-pyrrolidone (NMP) solvent was utilized to combine 90% active material (photocatalyst) and 10% binder agent (PVDF) to prepare a paste. Employing a doctor blade approach, the as-prepared paste was placed on the functionalized surface of the FTO glass. The decorated FTO was placed in an oven for 24 hours at 60 °C for drying properly. A tungsten lamp (100 W) was utilized to illuminate the prepared samples. N_2 gas was used to purge the electrolyte for 30 minutes prior to the tests. In a 0.5 M Na_2SO_4 solution, electrochemical impedance spectroscopy (EIS) was conducted at a frequency ranging from 0.1 Hz to 1000 Hz. In each instance, a sinusoidal potential amplitude of 5 mV was applied. Mott–Schottky plots were obtained utilizing the same setup (applied voltage: −0.5 V, frequency: 1000 Hz, AC voltage: 5 mV amplitude). Over the course of on–off cycle, the transient photocurrent responses were measured at 0 V potential bias *versus* Ag/AgCl.

2.8 Photocatalytic performance test

The schematic diagram of the experimental set up for photocatalytic CO_2 hydrogenation to CH_3OH under visible light is presented in Fig. S2. Utilizing the prepared catalyst, a cylindrical fixed-bed continuous-flow quartz-glass reactor was employed to measure the hydrogenation of CO_2 to CH_3OH. The reactor is made up of a 130 mm length and 8 mm diameter column. 1 g of photocatalyst (40–50 mesh) was installed in the middle part of the column almost 10 mm in length. By filling both sides of the photocatalyst bed with quartz wool, the catalyst bed remained fixed. The reactor was installed in a cylindrical glass furnace 4 cm away from the light source and linked to the gas inlet and outlet. An electric heater is fitted into the furnace to control the temperature of the reactor. A thermocouple is fitted in the furnace to measure the inside temperature of the furnace. A mass flow controller was employed to control the flow rate of the reactant gas mixture. For maintaining a specified pressure, a back-pressure controller was integrated into the gas line which was connected to the outlet. The reaction was carried out at atmospheric pressure under specific reaction conditions, with an N_2 flow, at temperatures up to 300 °C. After 3 h, H_2 (generated by electrolysis) and CO_2 (99.999%) were provided throughout the reaction. In all experiments using the reaction mixture, we used the ratio $H_2 : CO_2 = 3:1$ that reflects a stoichiometric equation for the CH_3OH synthesis reaction ($CO_2 + 3H_2 \rightarrow CH_3OH + H_2O$) and has been commonly used in related prior studies. The kinetic study on the reaction was carried out between 200 °C and 300 °C. The liquid phase products (CH_3OH) resulting from photocatalytic CO_2 reduction were collected in a cold trap and subsequently analyzed on a gas chromatograph (GC-2014, SHIMADZU) equipped with a flame ionization detector (FID). The production rate of CH_3OH in the hydrogenation of CO_2 was determined by using the following eqn (1):[35]

$$\text{CH}_3\text{OH yield rate} = \frac{\text{Amount of produced CH}_3\text{OH}}{\text{Mass of photocatalyst} \times \text{time duration}} \quad \mu\text{mol } g_{cat}^{-1}\ h^{-1} \tag{1}$$

The apparent quantum yield of the as-prepared Ag–Si/MgO/ZnO photocatalyst for CH_3OH production was evaluated by using the following eqn (2).[35]

Table 1 Calculation of the change in zero point energy and change in TS for various reactions in the CO_2 hydrogenation to CH_3OH pathways

Reactions	Equations for change in ZPE	Value of ΔZPE (eV)	Equations for change in *TS*	Value of *TΔS* (eV)
$CO_2 + H = COOH$	$\Delta ZPE = ZPE_{COOH} - (ZPE_{CO_2} + ZPE_H)$	0.005238155	$T\Delta S = TS_{COOH} - (TS_{CO_2} + TS_H)$	−1.01506546
$COOH + H = CO + H_2O$	$\Delta ZPE = ZPE_{CO} + ZPE_{H_2O} - (ZPE_{COOH} + ZPE_H)$	0.010259345	$T\Delta S = TS_{CO} + TS_{H_2O} - (TS_{COOH} + TS_H)$	0.83977502
$CO + H = HCO$	$\Delta ZPE = ZPE_{HCO} - (ZPE_{CO} + ZPE_H)$	−0.120043635	$T\Delta S = TS_{HCO} - (TS_{CO} + TS_H)$	−0.27203544
$HCO + H = H_2CO$	$\Delta ZPE = ZPE_{H_2CO} - (ZPE_{CO} + ZPE_H)$	−0.114836475	$T\Delta S = TS_{H_2CO} - (TS_{CO} + TS_H)$	−0.37171585
$H_2CO + H = H_3CO$	$\Delta ZPE = ZPE_{H_3CO} - (ZPE_{H_2CO} + ZPE_H)$	−0.132813575	$T\Delta S = TS_{H_3CO} - (TS_{H_2CO} + TS_H)$	−0.30651881
$H_3CO + H = CH_3OH$	$\Delta ZPE = ZPE_{CH_3OH} - (ZPE_{H_3CO} + ZPE_H)$	−0.084275405	$T\Delta S = TS_{CH_3OH} - (TS_{H_3CO} + TS_H)$	−0.33720159

Apparent quantum yield for CH_3OH,

$$AQY = \frac{6 \times \text{number of } CH_3OH \text{ molecules}}{\text{Number of incident photons}} \times 100\% = \frac{6 \times N_{CH_3OH} \times N_A}{I_i \times A \times \frac{\lambda}{hc} \times t} \times 100\% \quad (2)$$

where N_{CH_3OH} was defined as the number of moles of CH_3OH that were generated during the time interval t. Avogadro's number was taken as (6.023×10^{23} atoms per mol). The area of the surface on which the light was irradiated was denoted as A (m^2). Planck's constant, h was considered as (6.626×10^{-34} J s); and the speed of light, c was taken as 3×10^8 m s^{-1}. The time duration of light irradiation was represented as t (s). The wavelength of incident light, λ was measured by using a bandpass filter and was taken as $\lambda = 420$ nm. The average intensity of incident light, I_i, was measured by a suitable measuring instrument, such as a pyranometer, and was expressed in W m^{-2}.

2.9 Computational methods

The distribution of the electro-magnetic (EM) field over Si/ZnO, Si/MgO, Si/ZnO/MgO, and Ag–Si/ZnO/MgO is conducted using the finite-difference time-domain (FDTD) method. 630 nm is used as the simulated excitation wavelength of all nanostructures. Ag–Si/ZnO/MgO is modeled as follows: isolated Si, Si/MgO and Ag–Si/MgO NPs assemblies are placed on the surface of ZnO nanosheets, respectively. A plane wave propagating in the *z*-direction with an electric field parallel to the *x*-direction was selected to estimate the electric field distribution. The dielectric functions of Ag, Si, MgO, and ZnO were taken from the literature. Density functional theory (DFT) calculations were carried out using the DMol3 module within the Materials Studio software package. The interaction between ionic cores and valence electrons was modeled using the projector augmented-wave (PAW) formalism. The plane-wave basis set was constructed with a kinetic energy cutoff of 500 eV to ensure adequate convergence. Exchange–correlation effects were accounted for within the framework of the generalized gradient approximation (GGA), employing the Perdew–Burke–Ernzerhof (PBE) functional. Brillouin zone integrations were performed using Monkhorst–Pack *k*-point meshes. For the slab models considered, a final *k*-point mesh of $X \times Y \times 1$ was adopted, where X and Y were determined from the convergence tests. A single *k*-point was used along the surface normal due to the large vacuum spacing. Self-consistent field (SCF) cycles were converged to a tolerance of 1×10^{-5} eV per atom, with convergence thresholds of 0.1 eV $Å^{-1}$ for maximum forces and 5×10^{-3} Å for atomic displacements.

The Gibbs free energy for all reactions was obtained by using the following formula eqn (3):[36]

$$\Delta G = \Delta E + \Delta ZPE - T\Delta S \quad (3)$$

Here, ΔE denotes the total energy change calculated using Materials Studio, while ΔZPE and ΔS correspond to the variations in zero-point energy and entropy, respectively. The values of ΔE, ZPE, ΔZPE and $T\Delta S$ are calculated by using the following eqn (S1)–(S4). The change in zero point energy and change in TS for various reactions in CO_2 hydrogenation to CH_3OH are calculated by the pathways provided in Table 1.

The adsorption energy (E_{ads}) was calculated using the following expression:[37]

$$E_{ads} = E_{adsorbate+surface} - (E_{adsorbate} + E_{surface}) \quad (4)$$

where $E_{adsorbate+surface}$ is the total energy of the surface system after adsorption of the species, $E_{adsorbate}$ is the total energy of the free adsorbate, and $E_{surface}$ is the total energy of the pristine surface.

3. Results and discussion

The surface activation process for the Ag–Si/ZnO/MgO composite photocatalyst is shown in Fig. 1A. Scanning electron microscopy (SEM) analysis was employed to investigate the morphology of the fabricated Ag–Si/MgO/ZnO catalyst. The Ag–Si/MgO/ZnO catalyst exhibited densely packed, well-defined cuboidal/prismatic particles with faceted surfaces, indicative of high crystallinity and uniform growth. These particles exhibit a relatively narrow size distribution and form an aggregated network with close particle-to-particle contact, as depicted in Fig. 1B and C. The morphology of Ag–Si/MgO/ZnO catalysts was also studied using transmission electron microscopy (TEM).

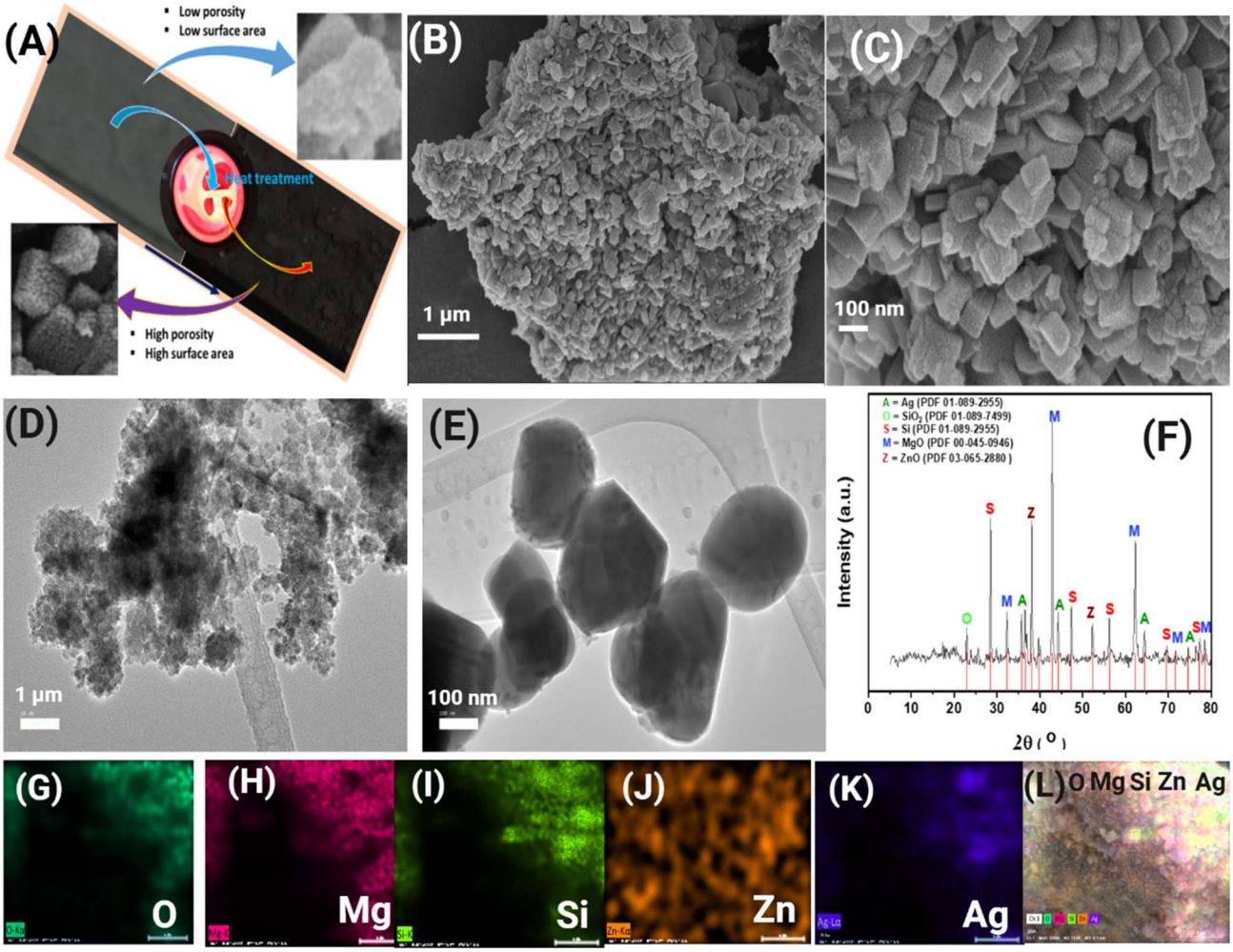

Fig. 1 Schematic diagram of the heat-induced surface activation process for the Ag–Si/ZnO/MgO composite photocatalyst (A); morphology of the as-prepared Ag–Si/MgO/ZnO blocks. SEM image of Ag–Si/MgO/ZnO (B and C); TEM images of Ag–Si/MgO/ZnO (D and E); XRD patterns of as-prepared Ag–Si/MgO/ZnO (F); elemental mapping of Ag–Si/MgO/ZnO by EDX analysis (G–L).

The TEM photograph shown in Fig. 1D and E displays particles that are well-defined and faceted. Their morphology is polyhedral and appears to be cuboidal or slightly truncated prismatic. The clear edges and uniform contrast show that these are single crystalline domains, not amorphous aggregates. The particle size seen in the TEM image is very similar to the size value proposed by SEM since the size is very monodispersed. Fig. 1G–L showing the EDX elemental mapping images of the synthesized Ag–Si/MgO/ZnO catalyst showed the distributions of elements Ag, Si, Zn, Mg, and O, thereby confirming successful preparation of the nanocomposite. The elemental mapping of the Ag–Si/MgO/ZnO nanostructured catalyst confirmed the uniform presence of Ag and Si on the nanocrystalline MgO/ZnO support, showing that these elements were evenly spread throughout the catalyst. The powder XRD analysis showed that all synthesized catalysts are highly crystalline. The XRD pattern of Ag–Si/MgO/ZnO shows peaks at 28.48°, 42.88°, 56.22°, 69.70°, and 77.38° depicting the indexed peaks (111), (220), (110), (400), and (331) of Si (JCPDS 01-089-2955). The presence of ZnO, MgO and Ag was confirmed by matching the characteristic peaks with their respective JCPDS files (03-65-2880, 00-045-0946, and 01-089-2955).

MgO promotion had been specifically important because MgO had provided basic sites that had strengthened CO_2 adsorption. A higher number of effective adsorption events was maintained compared with supports that were less basic or less able to stabilize highly dispersed metal particles.[38] The plasmonic function of Ag had increased the flux of energetic electrons under visible light, while MgO had increased reactant uptake and stabilized interfacial active sites, and this dual promotion had been consistent with the experimentally observed highest methanol rate (357.53 μmol g_{cat}^{-1} h^{-1} at 250 °C and 3 bar) and reduced apparent activation energy (158.14 kJ mol^{-1}) for Ag–Si/MgO/ZnO *versus* the Ag-free counterparts. It was inferred from these results that strong ZnO–MgO interactions occurred which generated a high dispersion of Ag and Si species on the surface of the catalyst and small active site formation.

All samples were studied under the same conditions using the same excitation wavelength of 450 nm in the solid phase to

study the charge-carrier dynamics and charge-separation efficiency using photoluminescence (PL) experiments (Fig. 2A). Lower PL intensity means charge separation is more efficient. There was a significantly lower number of recombination events in Ag–Si/MgO/ZnO indicating that the efficiency of charge-separation was excellent for this material. The introduction of Ag into Si/MgO/ZnO likely created additional vacancies that acted as traps for photo-generated charge carriers, thereby significantly suppressing their recombination. This property of keeping electrons in the conduction band for a longer period enhances their photocatalytic activity. The PL quenching effects seen in Ag–Si/MgO/ZnO showed that the charge transfer and separation in the system was enhanced. The outcomes of our PL tests have been confirmed to be consistent with the photocatalytic CO_2 reduction data (Fig. 4B, C and E). This means that effective suppression of photo-induced e^-/h^+ recombination results in enhanced observed activity. Ag–Si/MgO/ZnO showed the best performance for CH_3OH production among all tested samples.

Enhancing the photocatalytic conversion of CO_2 *via* the Ag–Si/MgO/ZnO heterostructure was due to efficient separation of photo-generated charge carriers. The presence of Ag in Ag–Si/

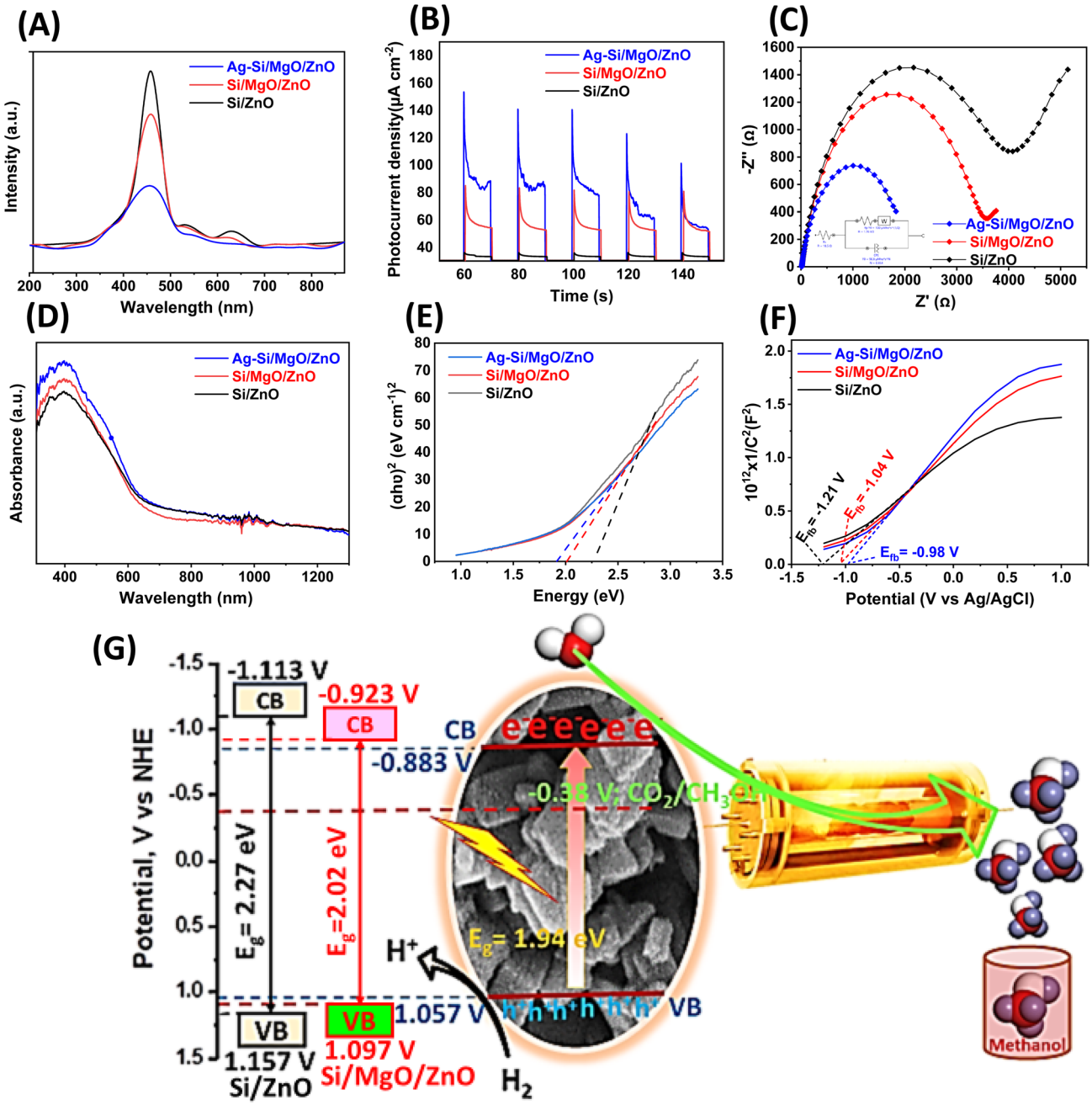

Fig. 2 (A) Photoluminescence (PL) spectra of Si/ZnO, Si/MgO/ZnO, and Ag–Si/MgO/ZnO; (B) transient photocurrent responses; (C) EIS plots; (D) UV-vis DRS; (E) Tauc plot of Si/ZnO, Si/MgO/ZnO, and Ag–Si/MgO/ZnO; (F) Mott–Schottky curves; and (G) band alignments of Si/ZnO, Si/MgO/ZnO, and Ag–Si/MgO/ZnO.

MgO/ZnO made the charge more mobile and limited e^-/h^+ recombination. As a result, the transient photocurrent response (Fig. 2B) of Ag–Si/MgO/ZnO was about 7.5 times stronger than that of Si/ZnO and 1.8 times stronger than that of Si/MgO/ZnO. The response of the photocurrent remains stable upon repeated on off cycles which indicates good photoelectrochemical stability that is in line with PL results. Fig. 2C presents EIS Nyquist plots (frequency range: 0.1 Hz to 1 kHz, applied bias: −0.5 V). A minor arc radius in the Nyquist plot suggested less resistance to electron migration, signifying efficient charge-carrier separation. The Ag–Si/MgO/ZnO composite had a smaller arc radius than Si/ZnO and Si/MgO/ZnO with less charge recombination and improved electron–hole migration efficiency. These results were in agreement with the PL spectra. It can be concluded that Ag may play a crucial role in enhancing charge-separation efficiency by suppressing charge-recombination rates and improving the light-absorption behavior. Other researchers also observed that Ag loading effectively suppressed photo-induced electron–hole recombination and increased visible-light absorption, ultimately enhancing photocatalytic activity.[39]

UV-vis diffuse reflectance spectrophotometry was used to study optical absorption characteristics of the prepared photocatalysts. The UV-vis diffuse reflectance spectra of Si/MgO/ZnO and Ag–Si/MgO/ZnO are presented in Fig. 2D. The absorption band edge of Si/MgO/ZnO is observed at about 600 nm. After adding Ag nanoparticles, the absorption peak in the visible range was increased as well as red-shifted to about 630 nm. Thus, the edge of absorption was changed. The main reason for this change was due to the SPR behavior of the Ag species. Thus, inclusion of Ag into Ag–Si/MgO/ZnO was found to have greatly enhanced the light-absorption range into the visible region. Similar observations were made by Chen *et al.* who realized that Ag doping is responsible for visible light absorption due to plasmon resonance.[39] A shift in UV-vis light absorption toward the visible region after Ag doping was also reported by Chen *et al.*[40] However, it was noted that excessive Ag loading resulted in a decline in light absorption and photocatalytic CO_2 reduction activity, likely due to a shielding effect, where surplus Ag partially blocked the light absorption of ZnO and MgO. The bandgap (E_g) values of the samples were estimated using Tauc's relation, as shown in eqn (5).[41]

$$\alpha h\nu = A(h\nu - E_g)^n \quad (5)$$

Here, A is a constant, E_g represents the semiconductor bandgap, and n is assigned a value of $\frac{1}{2}$ for a direct bandgap semiconductor. The plots of $(\alpha h\nu)^2$ *versus* photon energy are generated. In Fig. 2E, a straight line is fitted to the linear portion of the curve, and this line is extrapolated to the *X*-axis to determine the bandgap values. The band-gap values of Si/ZnO, Si/MgO/ZnO and Ag–Si/MgO/ZnO photocatalysts were derived from Fig. 2E as follows, 2.27, 2.02 and 1.94 eV, respectively. The bandgap of Ag–Si/MgO/ZnO is shifted to the left after loading of Ag and improved photocatalytic efficiency for CO_2 reduction. A suitable conduction band edge position and an adequate supply of free electrons were considered vital for achieving higher photocatalytic performance. Vu *et al.* suggested that the conduction band position should have been more negative than the reduction potential of CO_2 to CH_3OH (−0.38 V, NHE) in order to enable CH_3OH production.[42] In this context, Mott–Schottky analysis was carried out to determine the semiconductor type, and the flat-band potential (E_{fb}) was obtained (Fig. 2F). Si/ZnO, Si/MgO/ZnO and Ag–Si/MgO/ZnO samples exhibited positive slopes, indicating n-type semiconductor behavior.[43] The flat-band potentials (E_{fb}) of Si/ZnO, Si/MgO/ZnO and Ag–Si/MgO/ZnO were evaluated to be 1.21 V, −1.02 V and −0.98 V (*vs.* Ag/AgCl), respectively, from the Mott–Schottky plots. The E_{fb} values (*vs.* NHE) for both samples were calculated using eqn (6).[44]

$$E_{fb}\ (vs.\ \text{NHE}) = E_{fb}\ (vs.\ \text{Ag/AgCl}) + 0.197 \quad (6)$$

The values of E_{fb} (*vs.* NHE) for Si/ZnO, Si/MgO/ZnO and Ag–Si/MgO/ZnO samples were determined to be −1.013 V, −0.823 V and −0.783 V, respectively. It was known that the conduction band (CB) position of an n-type semiconductor lies approximately 0.1 eV below E_{fb}.[43] Hence, the CB potentials for Si/ZnO, Si/MgO/ZnO and Ag–Si/MgO/ZnO were calculated to be −1.113 V, −0.923 V and −0.883 V, respectively. The VB positions were then determined to be 1.157 V for Si/ZnO (−1.113 + 2.27), 1.097 V for Si/MgO/ZnO (−0.923 + 2.02) and 1.057 V for Ag–Si/MgO/ZnO (−0.883 + 1.94). Ag nanoparticles were found to act as electron-trapping centers, leading to enhanced photocatalytic performance.[39] Based on these calculations, experimental data, and CO_2 photoreduction results, a possible band diagram of the as-synthesized photocatalysts was proposed, and the mechanism of CO_2 photoreduction to CH_3OH over the Ag–Si/MgO/ZnO heterostructure was illustrated (Fig. 2G). The conduction band-edge potential of Ag–Si/MgO/ZnO was shown to be more negative than the reduction potential of CO_2 to CH_3OH. Furthermore, the bandgap of Ag–Si/MgO/ZnO was found to be smaller than that of Si/MgO/ZnO. Under visible light illumination, photo-generated electrons were efficiently transferred from the CB of Ag–Si/MgO/ZnO to the Ag NPs. The electrons accumulated on Ag NPs and then reduced CO_2 to CH_3OH. The difference in CO_2 photoreduction efficiency between Ag-undoped and Ag-doped Si/MgO/ZnO heterostructures confirmed that the electron transfer rate from Ag NPs to the adsorbed carbonate species was enhanced by Ag integration, which improved carrier separation and overall CO_2 photoreduction efficiency. Additionally, a synergistic effect between ZnO and MgO was postulated to suppress photo-induced charge recombination by transferring photo-generated species from ZnO to MgO within the heterostructure. Thus, the as-prepared Ag–Si/MgO/ZnO heterostructure was found to play a significant role in promoting CH_3OH formation by increasing its production rate. To further elucidate the hydrogenation pathway for CO_2 reduction to CH_3OH over the Ag–Si dual-metal active sites of the Ag–Si/MgO/ZnO catalyst, DFT calculations were carried out using the Material Studio software. The surface electronic state, chemical composition, and bonding environment of the synthesized catalysts were analyzed by X-ray photoelectron spectroscopy

(XPS). The XPS spectra of the Ag–Si/MgO/ZnO catalyst are presented in Fig. 3A–E. The full survey spectrum confirmed the presence of Ag, Si, Mg, Zn, and O elements within the sample, which was consistent with the EDS results, thereby indicating the successful synthesis of the catalyst. The characteristic peaks corresponding to Ag 3d, Si 2p, Mg 2p, Zn 2p, and O 1s were observed at their respective binding energies.

As shown in Fig. 3A, the Ag 3d spectrum exhibited two strong peaks at 367.7 and 374.4 eV, attributed to Ag $3d_{5/2}$ and Ag $3d_{3/2}$, respectively, confirming the presence of metallic Ag clusters. Two weak peaks corresponding to Ag^{+} were also observed, in agreement with the results of Tada *et al.*,[45] who reported that XPS spectra displayed peaks for metallic Ag at 368.0 eV (Ag $3d_{5/2}$) and 374.0 eV (Ag $3d_{3/2}$), as well as weak peaks for Ag^{+} at 369.7 eV (Ag $3d_{5/2}$) and 375.7 eV (Ag $3d_{3/2}$).[46,47] In the Si spectrum (Fig. 3B), peaks at 99.38 and 100.3 eV were assigned to Si $2p_{3/2}$ and Si $2p_{1/2}$, respectively, confirming the coexistence of Ag and Si in the composite. Cerofolini *et al.* reported that the $2p_{3/2}$ and $2p_{1/2}$ peaks in the range of 99–100.5 eV were characteristic of elemental silicon.[48] The peak at 100.3 eV was assigned to Si–H bonds, while a feature at 532.1 eV indicated the presence of Si–OH species. The presence of Si–H dangling bonds has been associated with enhanced charge separation efficiency on Si-supported photocatalysts.[49] These functional bonds acted as electron sinks, promoting charge transfer during photocatalysis. In the Mg spectrum (Fig. 3C), two peaks at 49.7 and 50.1 eV were attributed to Mg $2p_{3/2}$ and Mg $2p_{1/2}$, respectively. Fig. 3D shows the Zn 2p spectrum with peaks at 1021.24 eV and 1022.2 eV, corresponding to Zn $2p_{3/2}$ and Zn $2p_{1/2}$, confirming the coexistence of Zn^{2+} and Mg^{2+} species in the catalyst. A higher-binding-energy (~1023.5 eV) in the Zn $2p_{3/2}$ region could be attributed to surface-defective Zn^{2+} species, originating from oxygen-deficient coordination and/or hydroxylated Zn sites, which result in reduced electronic screening compared to bulk ZnO.[50] The O 1s spectrum (Fig. 3E) exhibited peaks at 529.7, 530.9, and 532.1 eV, assigned to lattice oxygen, oxygen vacancies, and surface hydroxyl groups, respectively. The 529.7 eV peak was consistent with MgO formed through solid-phase oxidation of Mg. The role of MgO as a support was attributed to its tunable acid–base properties, which regulate electron transfer between the support and active phase, as suggested by Julkapli *et al.*[51] Additionally, Meshkani *et al.* reported that Lewis basicity of MgO enhanced chemisorption of surface functional groups and promoted electron transport.[52] No detectable boron-related chemical states had been observed in the XPS spectra, indicating that residual boron-containing species were below the detection limit and negligible in the final material.

The total density of states (TDOS) for bimetallic Ag–Si/MgO/ZnO, single-metallic Si/MgO/ZnO, and Si/ZnO catalysts is presented in Fig. S3. The TDOS of bimetallic Ag–Si/MgO/ZnO exhibited a narrower bandgap compared to Si/MgO/ZnO and Si/ZnO, justifying its faster electron excitation and transfer to intermediate species. The bimetallic co-catalyst thus accelerated electron transport, enabling the six-electron reduction of CO_2 to CH_3OH. Projected partial density of states (PDOS) analysis (Fig. 3F) showed that the s-band center of Ag–Si/MgO/

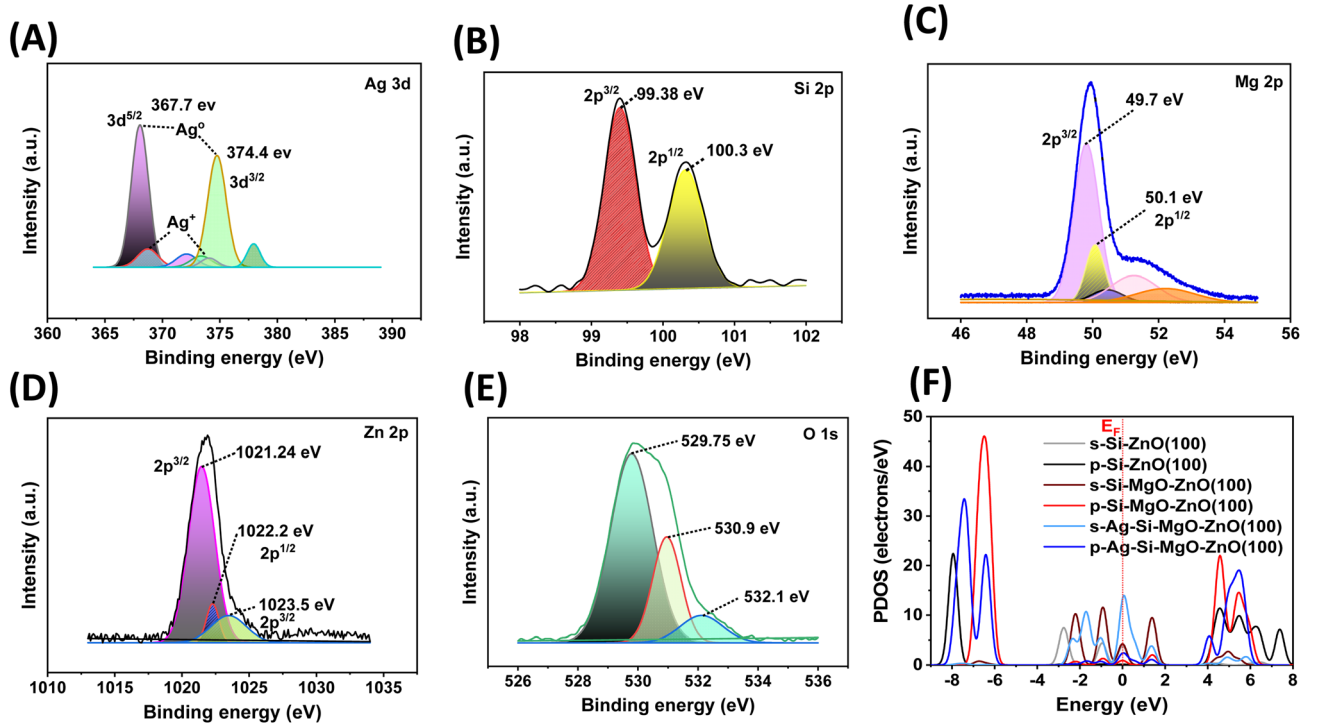

Fig. 3 XPS survey spectra of Ag–Si/MgO/ZnO; high-resolution XPS spectra of (A) Ag 3d, (B) Si 2p, (C) Mg 2p, (D) Zn 2p and (E) O 1s in the Ag–Si/MgO/ZnO sample. DFT calculations of CO_2 reduction. (F) The partial density of states for s and p-orbitals of Ag–Si/MgO/ZnO, Si/MgO/ZnO, and Si/ZnO.

ZnO was located near the Fermi level (E_F), favoring activation of O-species adsorption. The weak s–p orbital overlap indicated a long-range interlayer interaction, allowing CO_2 molecules to pass through easily without significantly affecting the catalyst interface.

To understand the enhancement in photocatalytic performance after loading Ag and Si nanoparticles, finite-difference time-domain (FDTD) calculations were conducted in the visible range at different wavelengths (400–800 nm) to simulate the local electric field distribution between the Ag and Si nanoparticle assemblies on MgO/ZnO with an interparticle distance of 2 nm (Fig. 4A and S4(A–F)). The electric field intensity distribution was visualized on a logarithmic scale. Fig. S4(G) shows the electric field distribution, $|E|^2$, around the surface of Ag–Si/MgO/ZnO as a function of wavelength using FDTD simulations. Upon light irradiation, the electric field distribution $|E|^2$ around the surface of Ag–Si/MgO/ZnO was enhanced, and a maximum value of $|E_{max}|^2$ of ≈800 was obtained at a wavelength of 457.143 nm. This improved local electric field, originating from the LSPR effect, was believed to have accelerated the transfer of hot electrons in the Ag–Si nanoparticles and promoted the separation of electron–hole pairs in MgO/ZnO. Furthermore, the visible-light absorbance was increased by Ag loading, thereby improving the photocatalytic activity, consistent with the photoluminescence results. The photocatalytic performance of the prepared samples was evaluated in a continuous-flow reactor system using CO_2 as the reactant at temperatures up to 300 °C and atmospheric pressure. The H_2/CO_2 ratio was maintained at 3 : 1. The results (Fig. 4B–F) showed that CH_3OH was the predominant product. At 160 °C, CH_3OH formation was detected under light irradiation, whereas no CH_3OH was observed under dark conditions. These results suggested that below 160 °C, the Ag–Si/MgO/ZnO nanocrystal superstructures could only catalyze the RWGS reaction. CH_3OH formation was most likely kinetically inhibited at low temperatures and pressures. The highest CH_3OH production rate was obtained at 250 °C, reaching 357.53 μmol g_{cat}^{-1} h^{-1} under light illumination (Fig. 4B and C). This value at 3 bar was higher than that produced over Si/MgO/ZnO and Si/ZnO composites by factors of 1.12 and 4.7, respectively. The as-prepared Ag–Si/MgO/ZnO photocatalyst exhibited a high apparent quantum yield (AQY) of 21.27% at an excitation wavelength of 420 nm for CH_3OH production, demonstrating its excellent visible-light-driven photocatalytic efficiency. When the temperature was increased to 300 °C, the CH_3OH production rate decreased to 121.84 μmol g_{cat}^{-1} h^{-1}. This decline was attributed to the exothermic nature of CH_3OH synthesis (eqn (1)), which shifted the equilibrium toward the reactants at

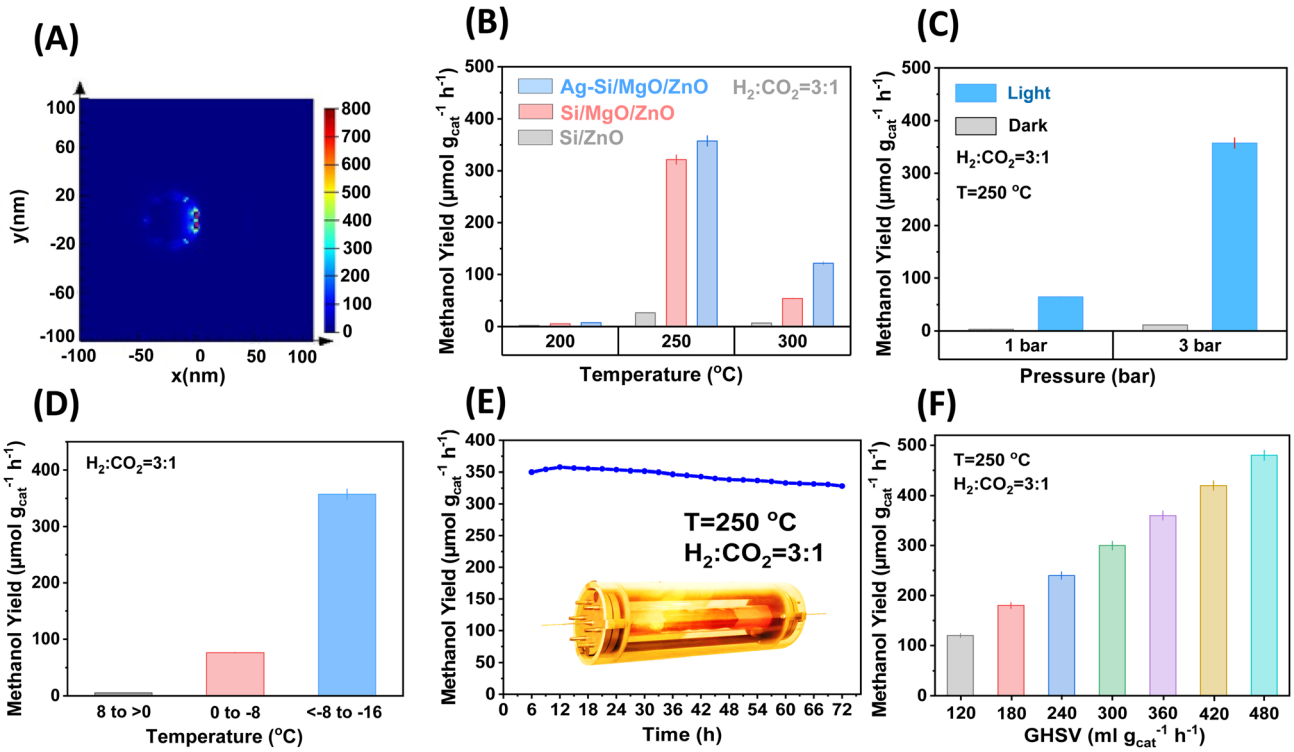

Fig. 4 (A) FDTD simulation of the electric field distributions, $|E|^2$ around the surface of Ag–Si nanoparticles placed on MgO/ZnO excited by visible light at a wavelength of 457.143 nm. Photo-thermo-catalytic performance: (B) temperature-dependent CH_3OH generation rate over Si/ZnO, Si/MgO/ZnO, and Ag–Si/MgO/ZnO photocatalysts under photo-thermal conditions. (C) Influence of pressure on the CH_3OH evolution rate over Ag–Si/MgO/ZnO under dark and light conditions; (D) influence of cooling temperature on methanol condensation in the reservoir; (E) stability performance of the Ag–Si/MgO/ZnO photocatalyst in photocatalytic CO_2 hydrogenation to CH_3OH for continuous 72 h at 250 °C and 3 bar pressure under irradiation of light; (F) methanol production rate as a function of GHSV over Ag–Si/MgO/ZnO; reaction conditions: 1 g of catalyst, 300 W lamp, 250 °C, and $H_2 : CO_2 = 3 : 1$ for (C, E and F).

higher temperatures according to Le Chatelier's principle. The reaction thermodynamics at 300 °C favored the RWGS pathway, confirming that 250 °C was the optimal temperature for CH_3OH formation.

A preliminary evaluation of the temperature-dependent solar CH_3OH production over Ag–Si/MgO/ZnO is shown in Fig. 4B. The largest amount of CH_3OH was condensed between −8 °C and −16 °C (Fig. 4D). The stability of the Ag–Si/MgO/ZnO photocatalyst was tested during continuous operation for 72 h at 250 °C and 3 bar under light irradiation (Fig. 4E). Only a slight decrease in the CH_3OH production rate was observed, indicating excellent long-term stability. CH_3OH production rates of various photocatalysts and comparable systems are listed in Table 2.[53–59] A significant enhancement of CH_3OH generation from 159.84 to 357.53 μmol g_{cat}^{-1} h^{-1} was achieved when the GHSV was increased from 120 to 480 mL g_{cat}^{-1} h^{-1} at 250 °C and 3 bar (Fig. 4F). This improvement was attributed to the synergistic effect of Ag–Si bimetallic loading, consistent with previous findings by Chen *et al.*,[40] who reported that Ag doping effectively suppressed electron–hole recombination and Si increased the catalyst surface area, jointly promoting visible-light photocatalysis. Plasmonic enhancement had been imparted by Ag because the optical response had been extended into the visible region and red-shifted toward ∼630 nm after Ag incorporation, and stronger charge separation/transport had been evidenced by pronounced PL quenching, higher transient photocurrent, and a smaller EIS semicircle, indicating that a larger fraction of photoexcited electrons had been delivered to surface reaction sites than in non-plasmonic semiconductor-only systems.[60] This behavior had contrasted with common strategies such as band-gap narrowing by bulk doping or simple heterojunction formation, where photon harvesting and interfacial electron flux had often remained limited by weak visible absorption or fast recombination; in the present architecture, plasmonic near-field/hot-carrier effects had been expected to increase the local excitation rate and accelerate interfacial electron injection under visible irradiation, thereby increasing the effective electron supply for CO_2/CO activation and hydrogenation.[61]

A schematic summary had been proposed in which CO_2 had been adsorbed at basic MgO sites, COOH*/CO* formation had been favored at Ag–Si/MgO/ZnO and terminal hydrogenation to CH_3OH completed predominantly at Ag sites supplied by efficiently separated photoelectrons under visible irradiation. The most favorable pathway for CO_2 hydrogenation to CH_3OH over this interface system was determined. Formate (HCOO*) and carboxyl (*COOH) species were identified as the key intermediates in the HCOO* and RWGS pathways. The Ag–Si/MgO/ZnO(100) system demonstrated the most energetically favorable *COOH pathway, with the lowest barrier (−4.93 eV) and a strongly exothermic reaction energy for CH_3OH formation (−8.55961 eV). In contrast, the HCOO* pathway exhibited a high barrier (15.1 eV) and endothermic CO_2 → HCOO* conversion. Therefore, the *COOH route was identified as the preferred pathway over Ag–Si/MgO/ZnO(100) (Fig. 5A). Starting from *COOH, the Gibbs free-energy profiles for the $6H^+/6e^-$ reduction of CO_2 to CH_3OH over Ag–Si/MgO/ZnO(100) and Si/MgO/ZnO(100) were analyzed (Fig. 5B). CO_2 hydrogenation to *COOH was exothermic (−4.93 eV) over Ag–Si/MgO/ZnO(100) but endothermic (+1.95 eV) over Si/MgO/ZnO(100), demonstrating the greater favorability of COOH formation in the presence of Ag. Incorporation of MgO enhanced *COOH adsorption, enabling its conversion to *CO, which was readily hydrogenated to methoxy (CH_3O*), as also reported by Li *et al.*[62] Compared with Si/MgO/ZnO, Ag–Si/MgO/ZnO had little effect on the free energies of *COOH → *CO, *CO → CHO, or *CHO → *CH_2O. However, the last three proton-transfer steps were identified as the decisive steps controlling performance. It was inferred that the first three intermediates were adsorbed on Si sites, while the final three were stabilized on Ag sites.

Partial density of states (PDOS) analysis at Ag sites demonstrated that Ag facilitated more rapid electron transfer from *CH_2O, accelerating its hydrogenation to *CH_3O. The free energy for the step $CH_3O + H^+ + e^- \rightarrow CH_3OH$ was reduced to 5.65 eV (Fig. 5B). Overall, CH_3OH formation over Ag–Si/MgO/ZnO proceeded predominantly *via* the pathway:

$$*COOH + H* \rightarrow *CO + H* \rightarrow *HCO + H* \rightarrow *H_2CO + H* \rightarrow *CH_3O + H* \rightarrow CH_3OH*$$

which was both kinetically and thermodynamically preferred. This mechanism aligns with the literature reported by Shan *et al.*,[63] where CO_2 was adsorbed and activated to CO_2*, subsequently forming COOH* and CO* and undergoing stepwise hydrogenation to CH_3OH. Both of the final steps were enhanced at the bimetallic sites, indicating that Ag–Si/MgO/ZnO enabled more efficient and selective CO_2 conversion to CH_3OH. The apparent activation energy for Ag–Si/MgO/ZnO was

Table 2 Comparison of heterogeneous photocatalysts for hydrogenation of CO_2 into CH_3OH

Catalysts	T	P	$V_{CO_2}:V_{H_2}$	Methanol yield	Reference
Au/In_2O_3	—	—	3 : 1	320 μmol g_{cat}^{-1} h^{-1}	53
$CaCu_3Ti_4O_{12}$	250 °C	8 bar	3 : 1	308.5 μmol g_{cat}^{-1} h^{-1}	54
Ru/In_2O_3	—	atmP	3 : 1	280.4 μmol g_{cat}^{-1} h^{-1}	55
Cu/ZnO	220 °C	atmP	2.5 : 1	127.8 μmol g^{-1} h^{-1}	56
$In_2O_{3-x}(OH)_y$-NR-14h	250 °C	atmP	3 : 1	97.30 μmol g_{cat}^{-1} h^{-1}	57
$CoO/Co/TiO_2$	120 °C	atmP	3 : 1	39.6 μmol g_{cat}^{-1} h^{-1}	58
$H_zIn_2O_{3-x}(OH)_y$	300 °C	atmP	3 : 1	31.2 μmol g_{cat}^{-1} h^{-1}	59
$H_zIn_2O_{3-x}(OH)_y$	250 °C	atmP	3 : 1	14.92 μmol g_{cat}^{-1} h^{-1}	59
Ag–Si/MgO/ZnO	250 °C	3 bar	3 : 1	357.53 μmol g_{cat}^{-1} h^{-1}	This work

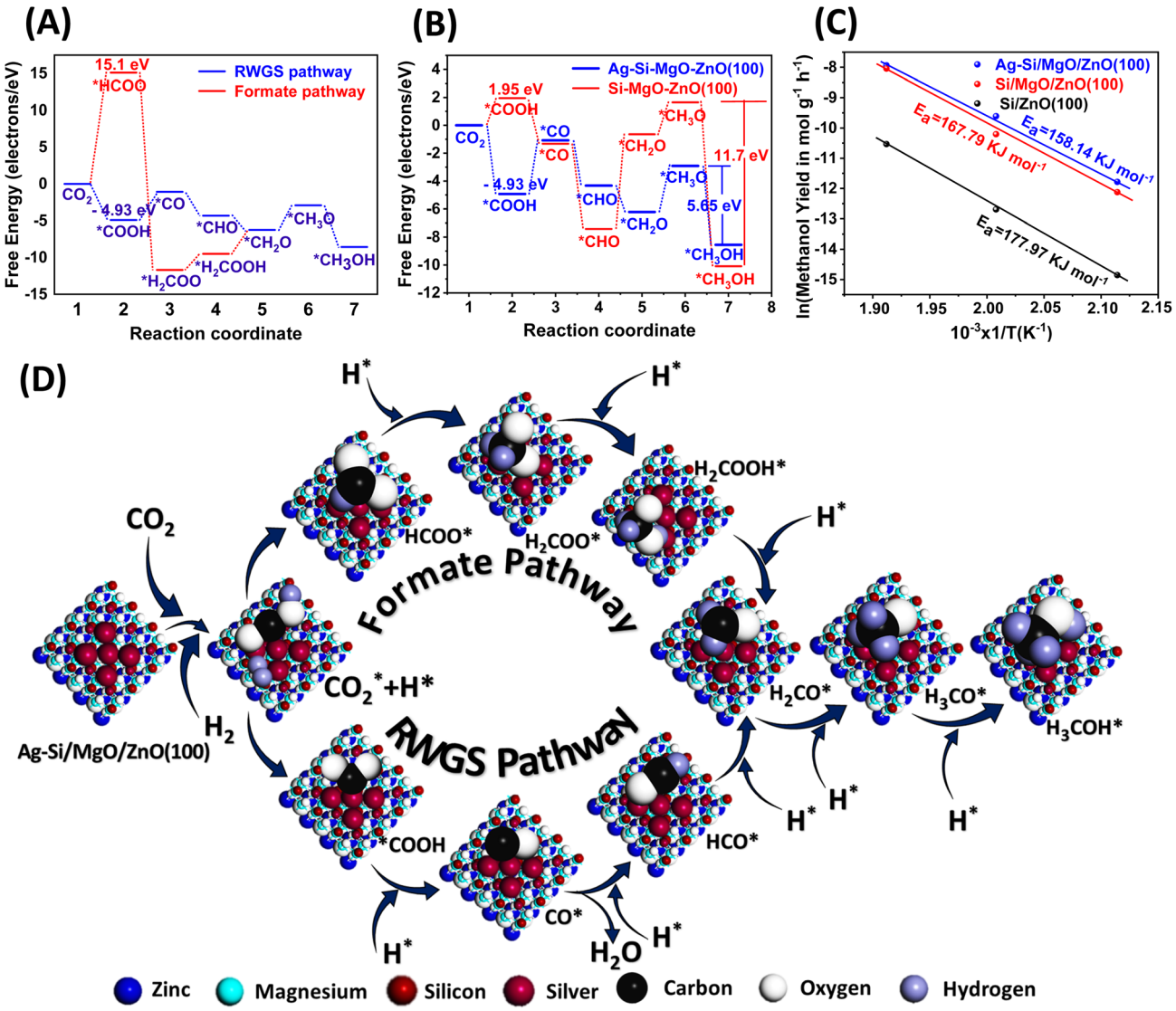

Fig. 5 DFT calculations of CO_2 reduction. (A) Free energy profiles of the reduction of CO_2 to CH_3OH in different pathways over Ag–Si/MgO/ZnO; (B) free energy profiles of the reduction of CO_2 to CH_3OH in the COOH pathway over Ag–Si/MgO/ZnO and Si/MgO/ZnO; (C) apparent activation energy (E_a) evaluated using Arrhenius plots based on hydrogenation of CO_2 into methanol under light conditions; (D) structural CO_2 hydrogenation pathways for methanol production within the Ag–Si/MgO/ZnO interface system.

158.14 kJ mol^{-1}, lower than that of Si/MgO/ZnO (167.79 kJ mol^{-1}) and Si/ZnO (177.97 kJ mol^{-1}) under light irradiation (Fig. 5C). In contrast, the apparent activation energy for Ag–Si/MgO/ZnO under purely thermal conditions as a reference was 172.48 kJ mol^{-1}, lower than that of Si/MgO/ZnO (184.51 kJ mol^{-1}) and Si/ZnO (201.38 kJ mol^{-1}) under dark conditions (Fig. S5). The apparent activation energy measured when the system is not exposed to light (under dark conditions) is termed as the apparent activation energy under purely thermal conditions. Because the reaction in this scenario is entirely driven by thermal energy, it is the appropriate baseline or reference condition to compare with the photo-catalytic conditions (under light irradiation). A comparison of the apparent activation energy (E_a) between light irradiation and dark conditions reveals that light significantly reduces the energy barrier for the reaction across all catalysts (Fig. 5C and S5). Under dark conditions, the reaction relies solely on thermal energy to overcome the activation barrier. The more significant values (172.48 kJ mol^{-1} to 201.38 kJ mol^{-1}) (Fig. S5) appear to be the substantial energy required to initiate the reaction without external photonic contribution. However, light irradiation consistently lowers the activation energy through generating electron–hole pairs by using photonic energy. These photo-induced charge-carriers efficiently reduce the thermal threshold needed to achieve the transition state, facilitating redox processes at the surface. In both circumstances, the synergistic impact of adding Ag and MgO further reduces this barrier. The observed reduction of E_a for Si/MgO/ZnO compared to Si/ZnO under both light and dark conditions was triggered by this modification that facilitated easier charge transfer and

provided more active sites. Ag can maintain a lower E_a than its non-doped counterparts in the dark by contributing to charge separation through defect levels. However, Ag acts as an electron sink, trapping photo-induced electrons to prevent their recombination with holes, which significantly boosted activity and lowered E_a under light conditions. The inclusion of Ag and Si bi-metals in the Ag–Si/MgO/ZnO catalyst creates a multifaceted enhancement that reduced activation energy (E_a) more effectively than single-metal systems. These results indicated that simultaneous Ag and Si doping significantly improved reactant activation. The DFT calculations were therefore consistent with the experimental activity trends.

Fig. 5D shows the structural CO_2 hydrogenation pathways for methanol production within the Ag–Si/MgO/ZnO interface system. Ag and Si had synergistically generated a dual-site catalytic landscape on Ag–Si/MgO/ZnO(100), where the initial CO_2 activation had been promoted through a COOH-mediated route that had been calculated as exothermic on Ag–Si/MgO/ZnO(100) (−4.93 eV) but endothermic on Si/MgO/ZnO(100) (+1.95 eV). This indicates that the bimetallic interface reduced the energy barrier for forming early oxygenated intermediates compared with the Ag-free surface. The decisive hydrogenation sequence had been described as spatially partitioned, such that early intermediates had been preferentially stabilized at Si-associated interfacial/oxide sites while the late hydrogenation steps (CHO* → CH_3OH) had been stabilized at Ag-rich sites acting as electron-accepting and hydrogenation centers, which had been consistent with the reported DOS features near the Fermi level.[64] This mechanistic assignment had been directly linked to experimental observables because suppressed recombination and improved charge transport had been evidenced by PL quenching, increased transient photocurrent, and a smaller EIS semicircle for Ag–Si/MgO/ZnO, and the same sample had delivered the highest methanol rate (357.53 μmol g_{cat}^{-1} h^{-1} at 250 °C and 3 bar) with the lowest apparent activation energy (158.14 kJ mol^{-1}), which had been aligned with the computed facilitation of key elementary steps.[65]

4. Conclusion

The Ag and Si–bimetal-doped MgO-promoted ZnO photocatalysts were synthesized *via* a solid-phase reaction approach. Using the 10 wt% Ag–Si/MgO/ZnO catalyst, the highest CH_3OH production rate of 357.53 μmol g_{cat}^{-1} h^{-1} was achieved for CO_2 hydrogenation at 250 °C under light illumination. A strong interaction between ZnO and MgO, resulting in a synergistic effect, could be responsible for the excellent selectivity of the 10 wt% Ag–Si/MgO/ZnO catalyst in the photocatalytic hydrogenation of CO_2 to CH_3OH. No significant deactivation was observed after 72 h of reaction. CO_2 adsorption on the Ag–Si/MgO/ZnO(100) surface (−1.04 eV) was 0.35 eV stronger than on Si/MgO/ZnO(100), which was inferred to have enhanced CO_2 activation and promoted higher CO_2 conversion. The stronger adsorption observed at the Ag–Si/MgO/ZnO(100) interface compared with the Si/MgO/ZnO(100) interface was inferred to enhance CO_2 adsorption, thereby promoting higher CO_2 conversion over the Ag–Si/MgO/ZnO(100) catalyst. This study thus provides new insights into the rational design of photocatalysts with well-defined heterojunctions for efficient photocatalytic CO_2 reduction.

Author contributions

AM: writing – original draft, methodology, formal analysis, data curation; A-TH: review & editing, writing; MTI: writing – review & editing, validation; MAH: writing – review & editing; TI: writing – review & editing, writing – original draft, visualization; AI: writing – review & editing, writing – original draft, supervision, funding acquisition, conceptualization.

Conflicts of interest

The authors declare that they have no known competing financial interests or personal relationships that could have appeared to influence the work reported in this paper.

Data availability

The data that support the findings of this study are available from the corresponding authors upon reasonable request.

Supplementary information (SI): schematic synthesis procedure of the Ag–Si/MgO/ZnO nanocomposite (S1); experimental setup for photocatalytic CO_2 hydrogenation to CH_3OH under visible light (S2); DFT calculations of CO_2 reduction and the total density of states for Ag–Si/MgO/ZnO, Si/MgO/ZnO, and Si/ZnO (S3); finite-difference time-domain (FDTD) simulation of electric field distribution (S4); apparent activation energy (E_a) evaluation (S5); and necessary equations. See DOI: https://doi.org/10.1039/d5se01485a.

Acknowledgements

This work was supported by the Bangladesh Energy and Power Research Council (BEPRC) under Research Grant No. March 27, 0000.000.39.001.17.651. The research was conducted at the Hydrogen Energy and CO_2 Conversion Laboratory, Department of Petroleum and Mining Engineering, Jashore University of Science and Technology, Jashore, 7408, Bangladesh.

References

1 P. Ndem, O. Biose, E. Effiong, S. Udegbe, J. E. Ukpebor, I. H. Ifijen and E. E. Ukpebor, *Environ. Monit. Assess.*, 2025, **197**(8), 925.
2 C. Zhang, J. Fang, Z. Han, P. Chen, X. Xu, K. Wang, Y. Shi and J. Liao, *iScience*, 2025, **28**(8), 113127.
3 F. Yan, H. Chen, T. Chi, J. Lu, X. Shen, F. Xie, P. Wang and Z. Zhang, *Chem. Eng. J.*, 2025, **520**, 166450.
4 J. He, G. Tian, D. Liao, Z. Li, Y. Cui, F. Wei, C. Zeng and C. Zhang, *J. Energy Chem.*, 2025, 778–803.
5 J. Zhao, Z. Wen, R. Zhu, Z. Li, R. Ding, Y. Zhu, T. Gu, R. Yang and Z. Zhu, *Chem. Eng. J. Adv.*, 2020, **3**, 100029.
6 A. Baig, V. Goswami and Sonal, *Asian J. Water, Environ. Pollut.*, 2024, **21**(6), 49–57.

7 F. A. Rafi, M. M. Rana, B. Agili and A. S. Al Shahrany, *Eur. J. Energy Res.*, 2025, **5**(2), 1–15.
8 M. M. Rana, S. M. Alam, F. A. Rafi, S. B. Deb, B. Agili, M. He and M. H. Ali, *IEEE Access*, 2025, 35124–35156.
9 M. M. Rana, F. A. Rafi, B. Agili and A. S. Al Shahrany, *Eur. J. Electr. Eng. Comput. Sci.*, 2024, **8**(2), 1–8.
10 S. Yasar Aurko, R. Salehdin, F. Allahma Rafi and K. Habibul Kabir, *The Fourth Industrial Revolution and Beyond: Select Proceedings of IC4IR+*, Springer Nature Singapore, Singapore, 2023, pp. 277–290.
11 Y. Yang, C. Shen, K. Sun, D. Mei and C. J. Liu, *ACS Catal.*, 2023, **13**(9), 6154–6168.
12 Q. Wu, S. Liang, T. Zhang, B. Louis and Q. Wang, *Fuel*, 2022, **313**, 122963.
13 C. Clavero, *Nat. Photonics*, 2014, **8**(2), 95–103.
14 M. M. J. Li and S. C. E. Tsang, *Catal. Sci. Technol.*, 2018, **8**(14), 3450–3464.
15 M. L. Brongersma, N. J. Halas and P. Nordlander, *Nat. Nanotechnol.*, 2015, **10**(1), 25–34.
16 S. M. Sze and K. K. Ng, *Physics of semiconductor devices: Sze/physics*, Wiley-Blackwell, Chichester, England, 3rd edn, 2006.
17 H. A. Atwater and A. Polman, *Nat. Mater.*, 2010, **9**(3), 205–213.
18 W. Sheng, J. Yang, X. Li, G. Liu, Z. Lin, J. Long, S. Xiao, L. Tan and Y. Chen, *Energy Environ. Sci.*, 2021, **14**(6), 3532–3541.
19 T. Kong, A. Liao, Y. Xu, X. Qiao, H. Zhang, L. Zhang and C. Zhang, *RSC Adv.*, 2024, **14**(24), 17041–17050.
20 J. Zhao, B. Liu, L. Meng, S. He, R. Yuan, Y. Hou, Z. Ding, H. Lin, Z. Zhang, X. Wang and J. Long, *Appl. Catal., B*, 2019, **256**, 117823.
21 A. O. Yusuf, R. Y. Tekle, H. K. Amusa and G. Palmisano, *Case Stud. Chem. Environ. Eng.*, 2025, **11**, 101172.
22 M. T. Khalil, X. Wu, S. Liu, Y. Liu, S. Ashraf, R. Shen, H. Zhang, Z. Peng, J. Jiang and B. Li, *Green Chem.*, 2025, **27**(30), 9016–9054.
23 Z. J. Wang, H. Song, H. Pang, Y. Ning, T. D. Dao, Z. Wang, H. Chen, Y. Weng, Q. Fu, T. Nagao and Y. Fang, *Appl. Catal., B*, 2019, **250**, 10–16.
24 J. L. G. Fierro, M. A. Peña and M. C. Alvarez-Galvan, *Supported Metal Catal.*, 2005, pp. 229–255.
25 V. D. Dasireddy and B. Likozar, *Renewable Energy*, 2019, **140**, 452–460.
26 Q. Chen, S. Meng, R. Liu, X. Zhai, X. Wang, L. Wang, H. Guo and Y. Yi, *Appl. Catal., B*, 2024, **342**, 123422.
27 Q. He, Z. Li, D. Li, F. Ning, Q. Wang, W. Liu, W. Zhang, Y. Cui, J. Zhang and C. Liu, *Mol. Catal.*, 2024, **558**, 114008.
28 Y. L. Men, Y. Liu, Q. Wang, Z. H. Luo, S. Shao, Y. B. Li and Y. X. Pan, *Chem. Eng. Sci.*, 2019, **200**, 167–175.
29 R. Pothu, H. Mitta, P. Banerjee, R. Boddula, R. K. Srivastava, P. K. Kalambate, R. Naik, A. B. Radwan and N. Al-Qahtani, *Mater. Sci. Energy Technol.*, 2023, **6**, 484–492.
30 K. Sun, N. Rui, C. Shen and C. J. Liu, *J. Phys. Chem. C*, 2021, **125**(20), 10926–10936.
31 H. Liu, M. Zhao, J. Guo, S. Sun, D. Li, D. He and Y. Lei, *ACS Sustainable Chem. Eng.*, 2025, **13**(15), 5787–5795.
32 X. Zhang, H. Liu, Y. Wang, S. Yang, Q. Chen, Z. Zhao, Y. Yang, Q. Kuang and Z. Xie, *Chem. Eng. J.*, 2022, **443**, 136482.
33 Y. Wang, Y. Liu, L. Tan, X. Lin, Y. Fang, X. F. Lu, Y. Hou, G. Zhang and S. Wang, *J. Mater. Chem. A*, 2023, **11**(48), 26804–26811.
34 Y. Wang, B. Su, S. Wang, L. Tan, G. Zhang, Y. Fang and X. Wang, *Angew. Chem., Int. Ed.*, 2025, e202508611.
35 A. Islam, S. H. Teo, M. R. Awual and Y. H. Taufiq-Yap, *J. Cleaner Prod.*, 2020, **244**, 118805.
36 C. Hu, Z. Jiang, Q. Wu, S. Cao, Q. Li, C. Chen, L. Yuan, W. Yang, J. Yang and J. Peng, *Nat. Commun.*, 2023, **14**(1), 4767.
37 H. Yu, F. Chen, X. Li, H. Huang, Q. Zhang, S. Su, K. Wang, E. Mao, B. Mei, G. Mul and T. Ma, *Nat. Commun.*, 2021, **12**(1), 4594.
38 H. J. Freund and G. Pacchioni, *Chem. Soc. Rev.*, 2008, **37**(10), 2224–2242.
39 S. Chen, B. Lv, D. Wu and Y. Xu, *J. Nanosci. Nanotechnol.*, 2013, **13**(2), 1569–1573.
40 Q. Chen, W. Shi, Y. Xu, D. Wu and Y. Sun, *Mater. Chem. Phys.*, 2011, **125**(3), 825–832.
41 I. H. Alsohaimi, A. M. Nassar, T. A. S. Elnasr and B. Amar Cheba, *J. Cleaner Prod.*, 2020, **248**, 119274.
42 N. N. Vu, S. Kaliaguine and T. O. Do, *Adv. Funct. Mater.*, 2019, **29**(31), 1901825.
43 N. Ojha, A. Bajpai and S. Kumar, *J. Colloid Interface Sci.*, 2021, **585**, 764–777.
44 N. Ojha, A. Bajpai and S. Kumar, *Catal. Sci. Technol.*, 2019, **9**(17), 4598–4613.
45 S. Tada, F. Watanabe, K. Kiyota, N. Shimoda, R. Hayashi, M. Takahashi, A. Nariyuki, A. Igarashi and S. Satokawa, *J. Catal.*, 2017, **351**, 107–118.
46 R. Grabowski, J. Słoczynski, M. Sliwa, D. Mucha, R. P. Socha, M. Lachowska and J. Skrzypek, *ACS Catal.*, 2011, **1**(4), 266–278.
47 I. C. Freitas, J. M. R. Gallo, J. M. C. Bueno and C. M. Marques, *Top. Catal.*, 2016, **59**(2), 357–365.
48 G. F. Cerofolini, C. Galati and L. Renna, *Surf. Interface Anal.*, 2003, **35**(12), 968–973.
49 S. H. Teo, A. Islam, Y. H. Taufiq-Yap and M. R. Awual, *J. Cleaner Prod.*, 2021, **313**, 127909.
50 P. Devaraji, M. Mapa, H. M. Abdul Hakkeem, V. Sudhakar, K. Krishnamoorthy and C. S. Gopinath, *ACS Omega*, 2017, **2**(10), 6768–6781.
51 N. M. Julkapli and S. Bagheri, *Rev. Inorg. Chem.*, 2016, **36**(1), 1–41.
52 F. Meshkani and M. Rezaei, *Catal. Commun.*, 2011, **12**(11), 1046–1050.
53 L. Wang, D. Yao, C. Zhang, Y. Chen, L. Amirav and Z. Zhong, *Chem Catal.*, 2024, **4**(9), 101095.
54 Z. Jiang, Z. Yuan, P. N. Duchesne, W. Sun, X. Lyu, W. Miao, C. J. Viasus Pérez, Y. Xu, D. Yang, B. Huang, Y. Dai, Z. Wang, H. He and G. A. Ozin, *Chem Catal.*, 2023, **3**(2), 100507.
55 B. Deng, H. Song, Q. Wang, J. Hong, S. Song, Y. Zhang, K. Peng, H. Zhang, T. Kako and J. Ye, *Appl. Catal., B*, 2023, **327**, 122471.

56 Z. J. Wang, H. Song, H. Pang, Y. Ning, T. D. Dao, Z. Wang, H. Chen, Y. Weng, Q. Fu, T. Nagao and Y. Fang, *Appl. Catal., B*, 2019, **250**, 10–16.
57 L. Wang, M. Ghoussoub, H. Wang, Y. Shao, W. Sun, A. A. Tountas, T. E. Wood, H. Li, J. Y. Y. Loh, Y. Dong and M. Xia, *Joule*, 2018, **2**(7), 1369–1381.
58 Z. H. He, C. S. Jiang, K. Wang, Z. Y. Wang, N. Li, W. T. Wang and Z. T. Liu, *Catal. Today*, 2020, **356**, 579–588.
59 Z. Zhang, C. Mao, D. M. Meira, P. N. Duchesne, A. A. Tountas, Z. Li, C. Qiu, S. Tang, R. Song, X. Ding and J. Sun, *Nat. Commun.*, 2022, **13**(1), 1512.
60 S. Linic, P. Christopher and D. B. Ingram, *Nat. Mater.*, 2011, **10**(12), 911–921.
61 M. L. Brongersma, N. J. Halas and P. Nordlander, *Nat. Nanotechnol.*, 2015, **10**(1), 25–34.
62 K. Li and J. G. Chen, *ACS Catal.*, 2019, **9**(9), 7840–7861.
63 X. Shan, G. Zhang, Y. Zhang, S. Zhang, F. Guo and Q. Xu, *Catalysts*, 2024, **14**(11), 756.
64 J. Greeley, T. F. Jaramillo, J. Bonde, I. B. Chorkendorff and J. K. Nørskov, *Nat. Mater.*, 2006, **5**(11), 909–913.
65 Z. Zeng, K. C. Chang, J. Kubal, N. M. Markovic and J. Greeley, *Nat. Energy*, 2017, **2**(6), 17070.